Biosensors and Bioelectronics 139 (2019) 111336

Contents lists available at ScienceDirect

Biosensors and Bioelectronics

journal homepage: www.elsevier.com/locate/bios

A wireless fully-passive acquisition of biopotentials

Shiyi Liu*, Xueling Meng, Jianwei Zhang, Junseok Chae

School of Electrical, Computer and Energy Engineering, Arizona State University, Tempe, AZ, USA

ARTICLE INFO

Keywords:
Fully-passive
Backscattering
ECG
EMG
EOG
Deep learning

ABSTRACT

Biopotential signals contain essential information for assessing functionality of organs and diagnosing diseases. We present a flexible sensor, capable of measuring biopotentials, in real time, in wireless and fully-passive manner. The flexible sensor collects and transmits biopotentials to an external reader without wire, battery, or harvesting/regulating element. The sensor is fabricated on a 90 µm-thick polyimide substrate with footprint of $18 \times 15 \times 0.5\,\text{mm}^3$. The wireless fully-passive acquisition of biopotentials is enabled by the RF (Radio Frequency) microwave backscattering effect where the biopotentials are modulated by an array of varactors with incoming RF carrier that is backscattered to the external reader. The flexile sensor is verified and validated by emulated signal and Electrocardiogram (ECG), Electromyogram (EMG), and Electrooculogram (EOG), respectively. A deep learning algorithm analyzes the signal quality of wirelessly acquired data, along with the data from commercially-available wired sensor counterparts. Wired and wireless data shows $< 3\%$ discrepancy in deep learning testing accuracy for ECG and EMG up to the wireless distance of 240 mm. Wireless acquisition of EOG further demonstrates accurate tracking of horizontal eye movement with deep learning training and testing accuracy reaching up to 93.6% and 92.2%, respectively, indicating successful detection of biopotentials signal as low as 250 μV_{PP}. These findings support that the real-time wireless fully-passive acquisition of on-body biopotentials is indeed feasible and may find various uses for future clinical research.

1. Introduction

Biopotentials provide vital information for physicians to exam the function of organs and diagnose abnormalities for subsequent treatment or more in-depth assessment actions. For example, Electrocardiogram (ECG) and Electromyogram (EMG), generated by heart and muscles, help to diagnose heart arrhythmias(Romhilt and Estes, 1968) and identiy neuromuscular disorders(Inbar and Noujaim, 1984), respectively; The inherent potential difference between the cornea and retina of eyes produce Electrooculogram (EOG), which is useful to study disorder of eye movement(Dey et al., 2012).

Biopotentials measurement often requires cables and wires that connect electrodes on individuals' skin to external bulky instrument and equipment for signal monitor and storage(Besnoff et al., 2013). The cumbersome cables and wires induce movement restriction and inconvenience to individuals, prohibiting long-term ambulatory monitoring of their physiological data. Commercialized wireless sensors alleviate the challenge, allowing wires-/cables-free acquisition of biopotentials. However, the vast majority of current commercialized wireless sensors rely on batteries to power electronics, resulting in a limited continuous collection of biopotentials. The state of art wireless sensors offer an average of merely one or two days operating time, primarily due to the high power consumption demanded by wireless communication protocols for data transmission(Dementyev and Smith, 2013). Biopotentials from one or two days of recording, such as ECG from Holter monitor, has been accepted by clinicians as an effective diagnosing tool. Some diseases or abnormalities, such as syncope and atrial fibrillation (AF), often require an extended long period of recording for months or even years to produce high diagnose yield(Israel et al., 2004; Thomsen et al., 2010). The lack of long-term continuous wireless biopotentials monitoring greatly limits the diagnose and study of those diseases or abnormalities.

To overcome the limitation of battery-powered wireless sensors, several research groups have reported wireless battery-free sensors, such as RFID (Radio Frequency Identification) technology-enabled wireless sensors(Besnoff et al., 2013; Dementyev and Smith, 2013; Philipose et al., 2005). These sensors contain sophisticated electronic circuitry that harvests power needed for operation, from such as inductive or RF coupling, thereby eliminating the demand for battery replacement. The recent highlights of such wireless battery-free sensors include flexible and light-weight, small-size epidermal electronics, having wireless communication capability, being the ideal form of

---

* Corresponding author.
E-mail address: Shiyi.liu.1@asu.edu (S. Liu).

https://doi.org/10.1016/j.bios.2019.111336
Received 1 March 2019; Received in revised form 13 May 2019; Accepted 16 May 2019
Available online 17 May 2019
0956-5663/

wearable electronics(Kim et al., 2016). Several recent studies have demonstrated epidermal electronics for measuring temperature(Kim et al., 2015), pulse(Kim et al., 2016) and electrophysiology(Xu et al., 2014). The Implementation that is closest to biopotential acquisition in a completely wireless, battery-free manner is the flexible epidermal electronics presented by Chung et al.(Chung et al., 2019), which uses inductive coils to harness power via inductive coupling. Unfortunately, wireless telemetry presented in those works suffers from the limited communication protocol, i.e., near field communication (NFC), or the stringent requirement of precise alignment of primary/secondary coils.

This work presents a small-size, light-weight, flexible sensor, capable of acquiring biopotentials in real time in a wireless and fully-passive manner, offering up to 240 mm wireless communication by consuming nearly zero power, except parasitics. RF backscattering wireless communication is used not to power the electronics on the sensor, but rather to allow bi-directional communication by reflecting the incident RF (Radio Frequency) wave. The sensor is fabricated on 90 µm-thick flexible polyimide substrate with a footprint of $18 \times 15 \times 0.5\,\text{mm}^3$, including all surface mount electronic components for wireless fully-passive telemetry of biopotentials. The term “fully-passive” denotes that the sensor is comprised entirely by passive components, i.e., batteries and power-consuming active circuitry are completely excluded. Several passive/fully-passive wireless biopotential sensors were reported(Seo et al., 2016; Wirdatmadja et al., 2016; Yeon et al., 2016), yet their functionalities were mostly validated by emulated signal(Wirdatmadja et al., 2016; Yeon et al., 2016) or evoked stimulation response(Seo et al., 2016). One notebale work is Neural Dust, a millimeter scale implantable wireless biopotential sensor based on ultrasound backscattering method(Seo et al., 2016). Utilizing acoustic wave as wireless transmission media, Neural Dust is miniaturized as small as $0.8 \times 3 \times 1\,\text{mm}^3$. Neural Dust showed its functionality at rather large amplitude ($> 2\text{mV}_{\text{pp}}$) neural signal. The wireless operating distance was reported to be rather short, 8.9 mm, and Neural Dust requires very accurate alignment to its external transceiver. Neural Dust also contains power consuming components such as resistor and transistors, thus it is passive, not fully-passive, wireless system. In contrast, our wireless sensor does not contain any active or resistive components, achieving near zero power consumption, for a fully-passive wireless system. Our sensor is unique as no work currently exists to acquire biopotentials using wearable sensors in a wireless and fully-passive manner; all previous work use batteries or other means of power supplying mechanisms to support electronics for wirelessly transmiting biopotentials from the body. We present wireless acquisition of various body biopotential, including ECG, EMG, and EOG of as low as $250\,\mu\text{V}_{\text{pp}}$, up to a maximum distance of 240 mm in a fully-passive manner. Our work may find applications in real time, long-term biopotential monitoring for various clinical diagnose and research purpose, in the form of small-size, flexible, epidermal or even implanted electronic systems.

2. Material and methods

2.1. Wireless fully-passive sensor

Fig. 1 shows simplified operating principle of the wireless system, comprising two sub-systems: 1) the wireless fully-passive sensor (Fig. 1a) for acquiring biopotentials and 2) the external interrogator (Fig. 1b) for wireless data readout and display. Wireless communication between the two sub-systems is accomplished by utilizing the RF backscattering effect, which was proposed in our previous works (Schwerdt et al., 2015, 2013, 2012, 2011). The differences between previous works and this work are discussed in details in supporting information. The external interrogator generates and radiates a single-tone sine wave RF carrier (f_0). When the RF carrier reaches the antenna on the wireless fully-passive sensor, a modulator, i.e., an array of varactor diodes, modulates the RF carrier with biopotentials (f_m) and antenna reflects the modulated signal back, backscattering, to the external interrogator. Among many harmonic components, the 3rd order mixing product ($2f_0 \pm f_m$) presents the highest SNR (signal-to-noise ratio, see supporting information), which goes through a series of filtering and demodulating process (Fig. 1b) to extract the original biopotential signals.

The backscattered power of 3rd order mixing products ($2f_0 \pm f_m$) can be obtained using:

$$P_3 = \frac{9C_0^2\gamma^2(1+\gamma)^2V_0^4V_m^2\omega_0^2R_r}{32V_j^4} \tag{1}$$

where V_0 is the amplitdue of RF carrier; ω_0 is the frequency of RF carrier; V_m is the amplitude of biopotentials; C_0 is zero-bias capacitance of the varactor diode; V_j is junction potential determined by material of the device; γ is gamma coefficient associated with doping parameter; R_r is the radiation resistance of antenna at $2f_0 \pm f_m$ (see supporting information for detailed derivation).

Equation (1) is the 1st order calculation which take little into account of other undesired harmonic products in the circuits. The frequency of RF carrier (f_0) is chosen as 2.33 GHz. The footprint of antenna on the sensor benefits from higher frequencies while the associated RF loss increases as a function of frequency. The trade-off between loss and antenna size is discussed in previous literature(Abbaspour-Tamijani et al., 2008). The antenna is constructed and simulated in High Frequency Structure Simulator (HFSS, Ansoft, figure S-1). Fig. 1c shows the schematic of equivalent circuit diagram of the sensor. The circuit is simulated using Advanced Design System (ADS, Keysight, figure S-2). The wireless fully-spassive sensor is fabricated with standard flexible PCB technology (figure S-3). Fully assembled senor has a total footprint of $18 \times 15 \times 0.5\,\text{mm}^3$. Fig. 1d shows photos of an assembled wireless fully-passive sensor, demonstrating its small size and high flexibility.

2.2. The external interrogator

Figure S-4a shows the detailed structure of the external interrogator. Output signal of external Interrogator is recorded by a Data Acquisition (DAQ) system (USB-6361, National instrument) at 360 (ECG) and 1000 (EMG and EOG) Hz sampling rates, respectively. The DAQ transfers the recorded biopotential data to an external PC, where they are digitally filtered before being displayed in a LabView (National Instrument). Three different types of biopotentials are considered as the measurement targets: ECG, EMG and EOG. Their amplitude and frequency range are listed in Table 1. Parameters of the digital filter are selected based on frequency characteristics of each type of biopotentials, which are detailed in the result section.

2.3. Study design

We studied the efficacy and accuracy of wireless fully-passive biopotential sensors to collect biopotentials such as ECG, EMG, and EOG. Ground truth measurements were taken by commercially-available sensors. To demonstrate the feasibility, we recruited volunteers to attach the wireless sensors on specific locations on their body to collect biopotentials. Randomization was not applicable and investigators were not blinded. All participants provided informed consent, and the studies were approved by the Arizona State University Institutional Review Board (IRB).

2.4. Biopotential recording protocols

The standard practice for ECG acquisition measures biopotentials at bipolar leads, (lead I, II, III in a three-electrode system), in which lead II is the most frequently viewed lead in clinical practice(Hockman et al., 1966) and is chosen as our target (Fig. 2a); EMG are measured at three commonly used muscles on participants’ limbs, including biceps

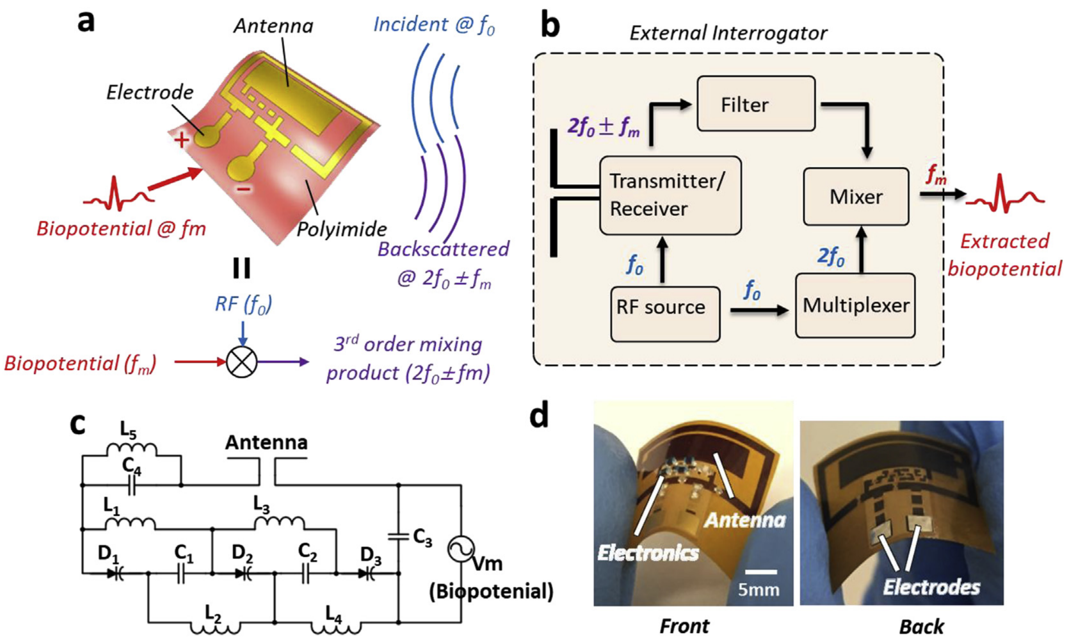

Figure 1. (a) Schematic of a simplified operating principle of wireless fully-passive sensor. The external interrogator generates and shines RF carrier (f_0) to the sensor. The antenna on the sensor receives the carrier and a modulator, varactor diodes, mixes the carrier with biopotentials (f_m) collected at the electrodes. The harmonic mixing products, including 3rd order ($2f_0 \pm f_m$), reflect back to the interrogator where the biopotential signals are extracted. (b) The simplified structure of external Interrogator. RF source generates the carrier (f_0) to be transmitted to the sensor as well as to be used in synchronous demodulation. The backscattered mixing products, including 3rd order ($2f_0 \pm f_m$), go through a series of filters and amplifiers to reach a down-converting mixer where the 3rd order product ($2f_0 \pm f_m$) is mixed with $2f_0$ to extract the biopotentials (f_m). (c) Equivalent electronic circuit model diagram of the sensor. Voltage source V_m represents low-frequency biopotentials (f_m) collected at the electrodes. (d) Photos of a fabricated and assembled sensor on a polyimide substrate, having footprint of $18 \times 15 \times 0.5\,\text{mm}^3$. The 65 µm-thick polyimide substrate contains antenna, discrete surface mount electronic components, and contact electrodes located at the backside to collect biopotentials.

Table 1
Amplitude and frequency range of target biopotentials.

Biopotentials	Amplitude Range	Frequency Range
Electrocardiogram (ECG)	1–5 mV	0.5–20 Hz
Electromyogram (EMG)	0.1–10 mV	50–200 Hz
Electrooculogram (EOG)	0.1–1 mV	0–30 Hz

brachii, extensor digitorum, and tibialis anterior, as shown in Fig. 3a; Fig. 4a shows the schematic setup to measure horizontal channel EOG signal (see supporting information for details).

2.5. Signal analysis by deep learning

Recent advances in deep learning technique have shown its promising potential in the field of biopotential signal analysis, such as ECG classification(Kiranyaz et al., 2016; Schmidhuber, 2015). Many studies have pointed out that the signal quality of raw data, inputted to deep learning models, has significant impact on final testing accuracy(Dodge and Karam, 2016; Karahan et al., 2016). A supervised deep learning algorithm is adopted in our study as a tool for signal quality comparison between the data from commercially-available wired sensors and that from the wireless fully-passive sensors.

We develop the deep learning algorithm using Keras on a PC. Various deep learning models on Keras are used to analyze the biopotentials. ECG and EMG, whose signal shape rather complex, require two 1D CNN layers with three full-connection dense layers. A simply-shaped EOG only demands three full-connection dense layers (figure S-7). Each model is trained by 30 epochs of training data set, followed by being tested with the testing data set to obtain testing accuracy. In addition, various slicing methods have been used, depending upon the characteristics of biopotentials and sampling frequency. Details of data set preparation are provided in supporting information.

3. Results and discussion

3.1. Bench top characterization

The verification of wireless fully-passive sensor is first performed on bench top. Figure S-4c shows the power of backscattered 3rd order product ($2f_0 + f_m$) increases as a function of RF carrier power at various distances (60 mm, 120 mm, 240 mm). The power spectrum measurement of the third order mixing product strongly supports that the wireless fully-passive telemetry benefits from RF backscattering methods. Power of backscattered product decreases by 13–15 dB as the transmission distance doubles, agreeing well with the EM wave free-space propagating model(Aning and Aning, 2012). For a 2 mV_{pp} sine wave input signal, the sensor demonstrates a working distance of 240 mm. The maximum working distance for the device to reliability measures actual biopotentials will be discussed in the next section. Figure S-4d shows the temporal waveforms of output at different input shape, including sine, square and triangle. All three differently shaped signals exhibit the minimum discrepancy with inputs, demonstrating the sensor's capability to reliably extract both simple (sine) and complicated (square and triangle) waveforms.

3.2. Electrocardiogram (ECG)

Fig. 2b shows normalized temporal ECG waveforms recorded from wireless fully-passive (red) and wired (blue) sensors, respectively, in a 3-s period. Both waveforms are filtered by 0.3–30 Hz band-path and 60 Hz notch filters. The signal distortion due to the filters may be negligible as ECG spans primarily 0.5–20 Hz(Lin, 2008). Correlation analysis between two waveforms produces a correlation coefficient as high as 0.8762, with a root-mean-square error (RMSE) as low as 0.0279. Both waveforms clearly show QRS complex and T wave. However, P wave, which has small amplitude of less than 250 μV_{pp}, is barely distinguishable in wireless recorded waveform. The wireless ECG

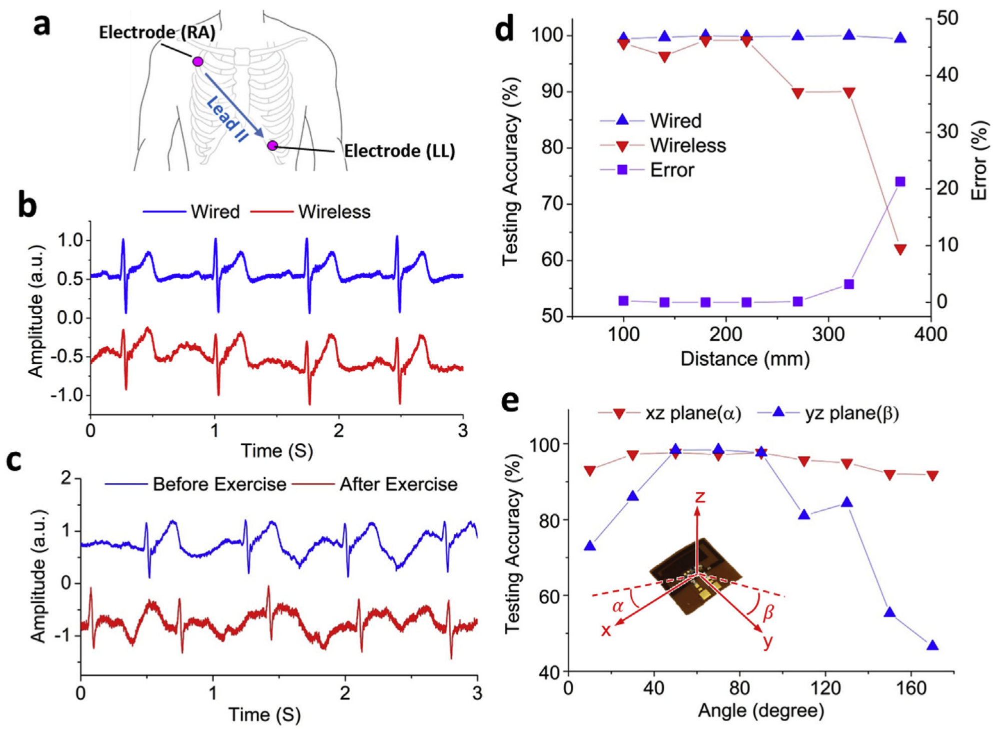

Fig. 2. Wireless fully-passive acquisition of Electrocardiogram (ECG). (a) Electrodes placement position for measuring lead II ECG. The two measurement electrodes RA (right arm) and LL (left leg) are connected to the wireless fully-passive sensor as well as a commercial wired sensor through electrical leads. A third electrode placed at the left shoulder (not shown in the plot) provides reference potential for the commercial sensor. (b) ECG recorded from the wireless fully-passive sensor in comparison with the output of the commercial wired ECG sensor that is recorded simultaneously. Both signals are normalized. The unit of amplitdue is arbitrary unit (a.u.) (c) Wireless fully-passive recording of ECG before/after the participant performs a 5-min running exercise. (d) Signal quality of wireless and wired ECG data as a function of wireless distances. Higher deep learning testing accuracy represents better signal quality, i.e., less noise and distortion. Error represents the percentage of miscounted heartbeat in wireless data, comparing to the wired counterpart. (e) Signal quality of wireless ECG data varies as a function of angle between external antenna and the sensor. Inlet shows the coordinate used in this measurement. The labelled angle represents the direction where external antenna locates.

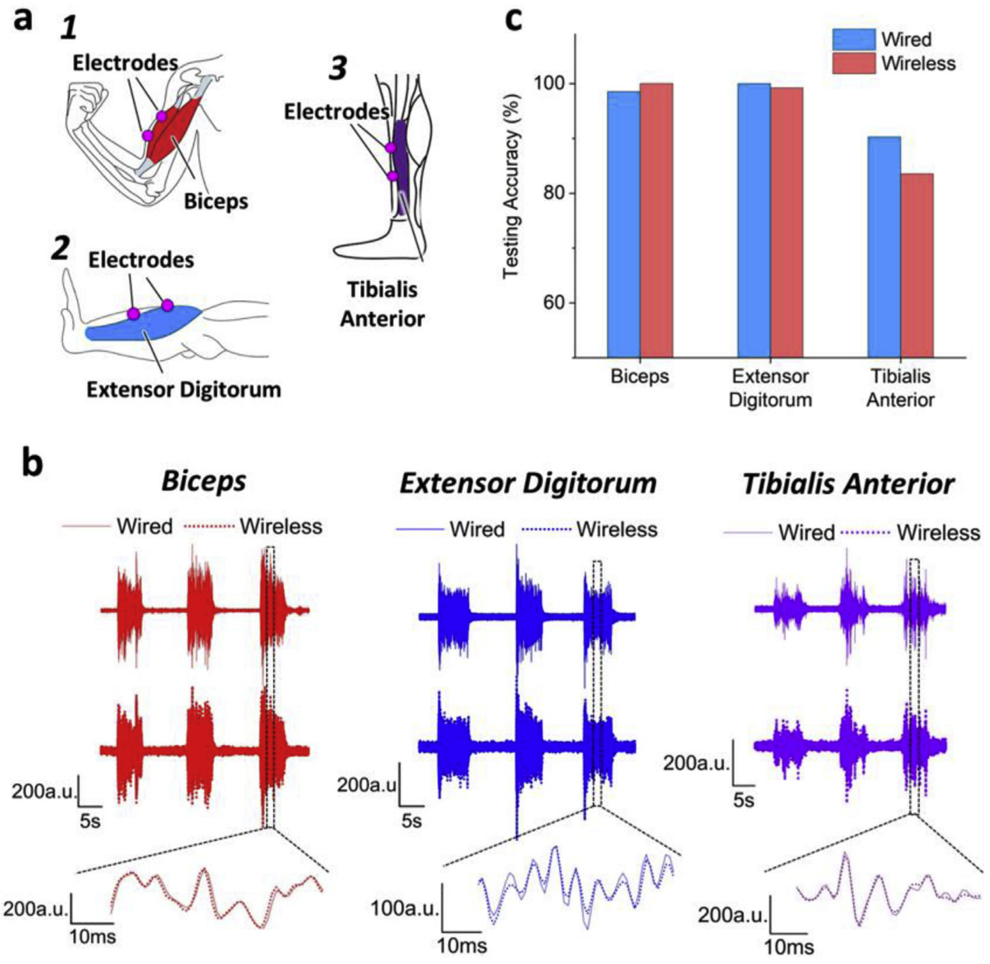

Fig. 3. Wireless fully-passive acquisition of Electromyography (EMG). (a) Schematic of electrodes placement for the EMG recording. Colored region highlights the targeting muscles, including biceps (red), extensor digitorum (blue), and tibialis anterior (violet). Electrodes are connected to the wireless sensor via electrical leads, together with a commercial wired sensor for simultaneous recording. (b) EMG signal of biceps (red), extensor digitorum (blue) and tibialis anterior (violet) from wired/wireless sensors during 45 s. Straight lines (top) represent EMG recorded from commercial wired sensor, while dotted lines (middle) depict their wireless counterparts. Bottom plots show zoom in of EMG signals in the marked regions. Data from wireless/wired sensors are normalized and aligned to demonstrate their closeness to each other. (c) EMG signal quality analysis by deep learning algorithm, which trains computer to distinguish EMG signal from noise. For each muscle, the training data set comes from 270 s of EMG recording. (For interpretation of the references to colour in this figure legend, the reader is referred to the Web version of this article.)

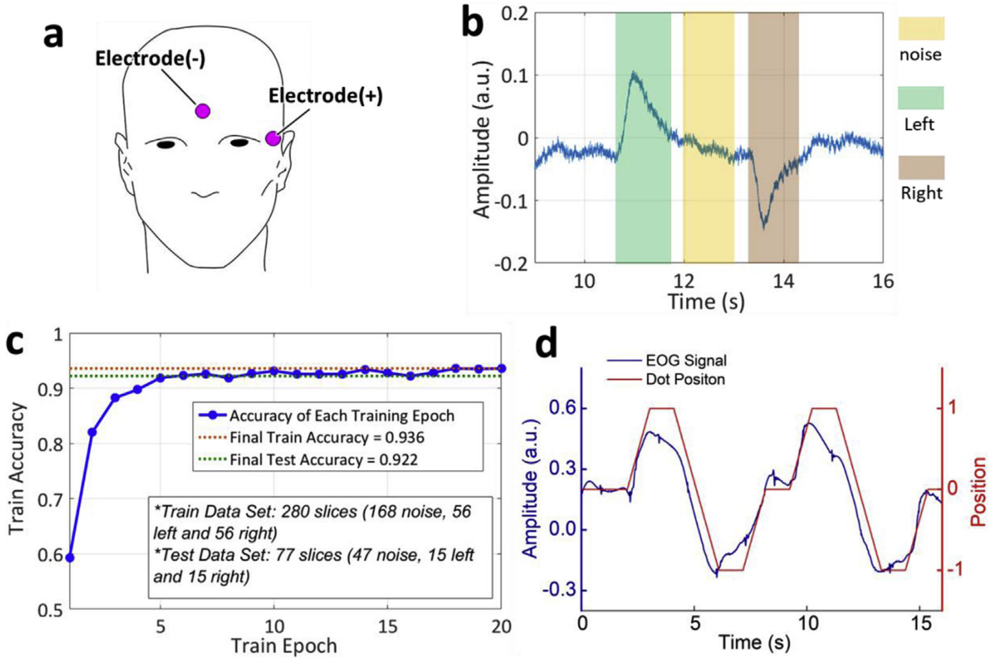

Fig. 4. Wireless fully-passive acquisition of Electrooculography (EOG). (a) Electrode location for measuring horizontal EOG. (b) Waveform of wireless recorded EOG signal when the participant moves his eyes left and right. Colored region represents the segment of data used to train deep learning model. (c) EOG signal analysis using deep learning algorithm. EOG Training data set is labelled as shown in (b). One training epoch represents one pass of complete data set into the deep learning training model. The inlet details the composition of training and testing data set. (d) Wireless recorded EOG signal of participant's eyes tracking a moving dot on computer screen. The target dot is programmed to perform horizontal movement within an 18.5 inches width computer monitor. The participant focuses his gazes upon the moving dot while EOG signal and the location of the dot are recorded simultaneously. Red line represents movement trail of the dot, where the location "0", "1" and "-1" represent center, left and right end of the monitor, respectively. (For interpretation of the references to colour in this figure legend, the reader is referred to the Web version of this article.)

data also exhibits a noticeable baseline distortion, possibly resulted from the breathing activity of participants. For temporal ECG features, measurement results from wired/wireless sensor show little discrepancy. For instance, QTc interval measured by wired and wireless sensor is 0.370 s and 0.362 s, respectively. The 8 ms difference is within the acceptable accuracy since the standard manual determination of QTc has an accuracy level of as large as 20–40 milli-sec(Goldenberg et al., 2006). This supports the wireless sensor may be useful for diagnosing of diseases and abnormalities such as Torsades de pointes (TdP)(Yap and Camm, 2003) and acute destabilized heart failure (ADHF)(Breidthardt et al., 2007).

To induce a change in heartbeat rhythm, the particiant performs a jogging practice at 6–7 km/h for 5 min. Heartbeat rate of the participant changes from 80/minutes to 94/minutes after the short-term running practice, as shown in Fig. 2c. The recorded wireless ECG data contains an undesirable baseline distortion introduced by breathing activity and other movement artifacts. The artifacts undoubtedly harm the ECG data integrity, impeding accurate feature extractions from recorded data. To reduce the effect of artifacts, a 16th-order polynomial fitting is adapted to remove baseline drifting curve (figure S-8).

The wireless fully-passive sensor is further evaluated by analyzing signal quality as a function of wireless transmission distance and angle. The ECG signal quality is assessed by using 1) the accuracy of heartbeat rate measurement and 2) the testing accuracy of applied deep-learning model which distinguishes ECG features from background noise. Fig. 2d shows the testing accuracy and error as the wireless transmission distance varies from 100 mm to 370 mm. At a given distance, both commercial wired sensor and wireless fully-passive sensor record participants' ECG continuously for 10 min. The numbers of heartbeat in each group of data are counted and compared. Within 270 mm distance, wireless heartbeat measurement shows very small errors ($< 0.5\%$) during the continuous 10 min recording. The heartbeat miscount occurs only once or twice in approximately seven hundred times when the QRS features are shadowed by artifacts. At distances larger than 270 mm, the heartbeat measurement error of wireless sensor exhibits exponential increase, which is primarily due to the SNR loss. Meanwhile, deep learning analysis reveals that when the distance remains less than 240 mm, testing accuracy of wireless ECG is comparable to that of the wired counterpart, with $< 3\%$ discrepancy. At over 240 mm distance, such discrepancy amplifies more than three times, resulting from testing accuracy of wireless data dropping to below 90%. As distances increase over 320 mm, the testing accuracy of wireless data suffers a sudden drop to as low as 60%, suggesting a significant degradation of ECG data quality.

A further observation at ECG temporal profile shows that drop of deep learning testing accuracy may correlate to the amplitude of signal, artifacts and noise (figure S-9). Below 240 mm, the ECG features are easily distinguishable from the wireless data. The artifacts exist, yet their amplitudes are insignificant comparing to that of target signal. Over 240 mm, as signal amplitude attenuates, the artifacts begin to dominate the waveform. When the distance reaches beyond 320 mm, the SNR drops to a level that features of ECG (P, QRS, and T wave) become almost indistinguishable from noise and artifacts. Thus, we summarize that the wireless fully-passive sensor has a working distance of 240 mm, where the sensor maintains its best performance in both heartbeat detection and deep learning analysis. Due to the elimination of any kind of power source on the sensor, our operating distance cannot compete with what offered by battery-powered devices. Comparing to other recently developed battery-free, flexible sensors that have similar footprints(Fonseca et al., 2006; Kim et al., 2016; Xu et al., 2014), our sensor achieves the highest operating distance. This attractive feature may facilitate the application of the sensor in more practical settings.

Signal quality of ECG is also a function of antenna radiation angle, the angle between external antenna and on-chip antenna on the wireless fully-passive sensor. Both the sensor and external antenna are designed to have maximum gain in perpendicular to their radiation plan (90°, z-axis in Fig. 2e). Fig. 2e shows the variation of deep learning testing accuracy as the radiation angle changes in two vertical planes (XZ plane and YZ plane), at a given distance of 140 mm. The testing accuracy in XZ plane is rather independent of angle change, maintaining $> 90\%$ for the entire angle span (0–180°). In YZ plane, testing accuracy exhibits strong dependency on angle arrangement, achieving the best results in the range of 50–90°. Different angular response in the two vertical planes possibly originates from intrinsic radiation pattern of the external dual-band antenna (A10194, Antenova).

3.3. Electromyogram (EMG)

Fig. 3b shows normalized wired/wireless EMG waveforms measured at biceps brachii, extensor digitorum and tibialis anterior muscle, respectively, during one cycle of the muscle contraction practice. For all cases, wireless EMG show excellent correspondence with the wired counterparts. Zooming in on the waveforms further reveals wireless data almost overlap with wired data. The good correspondence between wired and wireless data comes primarily from the remarkable reduction of low-frequency noise and motion artifacts, which are filtered out by the 20 Hz high-pass filter, thereby improving the wireless signal fidelity. It should also be noted that during the 6 cycles of muscle contraction practices, EMG data recorded from the three cases exhibit different SNRs. As shown in Supplementary Tables S–1, EMG measured at biceps brachii have the best signal quality, where wired and wireless data achieve an average SNR of 25 and 21 dB, respectively. In comparison, the average SNRs at extensor digitorum are 16 dB and 14 dB for wired and wireless measurements, respectively. At tibialis anterior muscles, the average SNRs become 7 dB (wired) and 6 dB (wireless), and only 1 in 6 cycles EMG data achieve the SNR over 10 dB. The degradation of signal quality at tibialis anterior muscle may be explained by uncertainties of electrodes location over or across the innervation zone. Previous studies(Rainoldi et al., 2004; Saitou et al., 2000) have shown that amplitude of the EMG signal reaches lowest when electrodes are placed over innervation zone. Moreover, different individuals may have different innervation zone distribution(Saitou et al., 2000).

Signal quality of wired and wireless EMG data is further quantified by deep learning analysis. Fig. 3c shows the quality assessment of EMG data using deep learning testing accuracy. At biceps brachii and extensor digitorum muscles, both wired and wireless EMG data show very high (> 98.5%) testing accuracy, indicating that at these two muscles, the wired and wireless sensors produce high-quality EMG data, well distinguished from noise. A decrease of EMG SNR from to 21-25 dB to 14–16 dB, in deep learning algorithm, does not yield significant difference in testing accuracy. At tibialis anterior, however, a clear drop of testing accuracy is observed. The wired and wireless EMG signal testing accuracy decrease by 10% and 17%, respectively. It is obvious that SNR degradation from to 14-16 dB to 6–7 dB has resulted in difficulty for the deep learning model to identify EMG signal from noise. Comparing with the case of extensor digitorum, although wired and wireless EMG data of tibialis anterior exhibit less discrepancy in SNR, 1 dB over 2 dB, their discrepancy in testing accuracy actually increases from 1.5% to 7%, suggesting that deterioration of signal quality in wireless EMG data is larger than that in the wired counterpart. Those results support that wireless sensor delivers EMG measurement accuracy for signal with SNR of 14 dB or above.

In application such as neuroprosthesis or movement recognition, feature extraction is an essential step in EMG signal analysis. To evaluate the potential implementation of wireless sensor in those fields, we compare four commonly used features extracted from wired and wireless EMG of biceps brachii, extensor digitorum, and tibialis anterior muscles. These features include(Chan and Green, 2017; Phinyomark et al., 2012; Zardoshti-Kermani et al., 1995): mean absolute value (MAV), root mean square (RMS), integral of absolute value (IAV), and wavelength (WL), listed in supplementary table (Tables S–1). MAV, RMS, and IAV of all three cases show very small errors (< 3%) between wired and wireless results. On the other hand, WL of wireless EMG shows a significant increase of error at tibialis anterior, 25%, as compared with the other two muscles cases, < 8%, suggesting feature extraction accuracy of the wireless sensor drops when measurement signal has low SNR. This result agrees well with the deep learning analysis in the previous section. Therefore, we conclude that wireless sensor is capable of reliable EMG acquisition upon SNR of over 14 dB. For such EMG signals, the wireless sensor may offer high accuracy, less than 8% error, so that EMG features can be used in EMG pattern recognition. Further study needs to be performed to confirm the practical implementation of the sensor, which will remain as our future work.

3.4. Electrooculogram (EOG)

EOG measures the inherent electrical potential between cornea and retina(Bulling et al., 2011). This potential changes as eye move, producing the EOG signal which can be used to track eye movement. Fig. 4b shows the normalized EOG signal when the participant rotates his eyeballs left and right, performing saccade. The angle of this rotation, according to previous studies, is approximately 60°(Darrell and Pentland, 1993). The recorded signal is filtered by a 3–30 Hz band-pass filter to reduce baseline shifting. As a participant rotates his eyeball left, the EOG shows a sharp increase of electrical potential, which gradually declines when movement of eyeball stops. As the participant rotates eyeballs right, EOG demonstrates the opposite trend. According to reference article(Bulling et al., 2011), amplitude of EOG signal is typically 5–20 μV_{pp}/degree, suggesting the wireless sensor is capable of measuring EOG signal in the range of 0.12–1.2 mV_{pp}, generated by 60 degrees of eyes movement.

The quality of EOG signal is analyzed using deep learning algorithm. To guarantee sufficient window length, left and right eyes movements are labelled in Fig. 4b. One complete left and right movement feature includes both the sudden rise and fall of the signal and the gradual recover that follows. When the EOG signal stabilizes, it is labelled as noise. Fig. 4c shows the process of training the deep learning model using the wireless measured EOG data. The training accuracy improves very quickly with the increase of training epochs, and only 5 epochs are required from beginning to close convergence. This fast training suggests that the EOG data collected by wireless sensor have high-quality so that they are learned by the deep learning model easily. Training accuracy reaches a maximum value of 93.6% while the testing accuracy achieves as high as 92.2%, which further validates the performance of the deep learning model trained by our wireless data(Hsu et al., 2003).

A real-time tracking trial is performed by using a pre-programmed dot moving on a computer screen. Fig. 4d shows that EOG signal closely follows the path of moving target. The position change of target dot from 0 to 1 corresponds to approximately 18 degrees of eye rotation, demonstrating the wireless sensor successfully records EOG signal as low as ~250 μV_{pp}. It should be noted the successful detection of EOG largely contributes to the sensor being placed off the body as well as the external antenna being located relatively close to the sensor, 30 mm. When the sensor, however, sits on body and the wireless transmission distance becomes large, detecting weak biopotentials, ~250 μV_{pp}, is a challenge, as shown by the P wave in ECG measurement (Fig. 2). The recorded EOG waveform also shows that amplitude of EOG signal changes even when the eyeball remains at a fixed location. Previous studies have reported similar baseline drift with commercially-available wired EOG recording equipment. (Belov et al., 2010; Bulling et al., 2011; Iwasaki et al., 2005). The causes of such phenomenon include change of skin resistance (Heide et al., 1999), electrode polarization, and background interfering (Bulling et al., 2011).

3.5. Disscusion

The sensor presented in this work is intended to be placed on participants' skin for the measurement of body potentials. −30–50 °C may be considered as reasonable temperature range, which falls within the general operating range of all the passive electronic components (varactors, inductors and capacitors) of the sensor. For −30–50 °C temperature range, the temperature has little impact on the value of the passive components due to the extremely low temperature coefficients (Cockbain and Harrop, 1968; Groves et al., 1996). Consequently the temperature effect has little impact on the performance of our sensor. We encapsulated the entire sensor by 10 μm-thick parylene-C, thus the humidity effect may not be very large as well.

The antenna radiation pattern is dependent upon the permittivity of its surrounding material. When humidity changes from 0 to 100% the permittivity of air remains almost constant (Zarnik and Belavic, 2012), suggesting the antenna performance may remain relatively unchanged as a function of humidity. A prior study has also shown that temperature change from − 30 to 60 °C results in merely 0.2 dB variation on the antenna gain (Mayer et al., 2001).

The overall cost of current system is primarily dominated by the equipment used in external interrogator. However, the cost can be substantially reduced by replacing the equipment with custom-designed monolithic microwave integrated circuit (MMIC). The antenna of the sensor can be further miniaturized by adapting 3D printing technology to print sophisticated 3D antenna structure. This may allow us to minimize the footprint of antenna while maintaining or even enhancing its performance. Beside biopotential recording, the sensor presented in this work may also find applications in other research field such as cultured cell stimulation or AC impedance measurement(Liu et al., 2017; Pan et al., 2019; Zou et al., 2016). Having near-zero power consumption, the sensor may be attractive for many biosensing applications where temperature change needs to be minimized, such as Surface Plasmonic Resonance (SPR)(Choi and Chae, 2009; Wang et al., 2014, 2011). These may be our future work.

4. Conclusion

In this paper, we demonstrated wireless fully-passive acquisition of various biopotentials, including ECG, EMG, and EOG. In ECG and EMG, data of the wireless sensor show good agreement with those from commercial wired sensors, maintaining < 3% discrepancy in deep learning testing accuracy, up to 240 mm wireless distance. Wireless EOG further demonstrates accurate tracking of participant's eyes movement, with deep learning algorithm achieving 93.6% and 92.2% training and testing accuracy, respectively. These results strongly support that the wireless fully-passive sensor is capable of accurately measuring body biopotentials with amplitude as low as 250 μV_{pp} and frequency up to 100 s Hz. Several technical challenges remain to be addressed, including signal's susceptibility to external environmental disturbance. Future work will focus on reducing the effect of artifacts and expanding the recording channels.

Declaration of interests

The authors declare that they have no known competing financial interests or personal relationships that could have appeared to influence the work reported in this paper.

The authors declare the following financial interests/personal relationships which may be considered as potential competing interests:

Competing interests

The authors declare no competing interest.

CRediT authorship contribution statement

Shiyi Liu: Writing - original draft. **Xueling Meng:** Methodology, Software. **Jianwei Zhang:** Formal analysis, Writing - review & editing. **Junseok Chae:** Supervision, Writing - review & editing.

Acknowledgement

This work was supported by National Science Foundation award 1344928.

Appendix A. Supplementary data

Supplementary data to this article can be found online at https://doi.org/10.1016/j.bios.2019.111336.

References

Abbaspour-Tamijani, A., Farooqui, M.F., Towe, B.C., Chae, J., 2008. A miniature fully-passive microwave back-scattering device for short-range telemetry of neural potentials. In: 2008 30th Annual International Conference of the IEEE Engineering in Medicine and Biology Society. Presented at the 2008 30th Annual International Conference of the IEEE Engineering in Medicine and Biology Society, pp. 129–132. https://doi.org/10.1109/IEMBS.2008.4649107.

Aning, M., Aning, M., 2012. Wireless Receiver Design for Digital Communications. SciTech Pub.

Belov, D.P., Eram, S.Y., Kolodyazhnyi, S.F., Kanunikov, I.E., Getmanenko, O.V., 2010. Electrooculogram detection of eye movements on gaze displacement. Neurosci. Behav. Physiol. 40, 583–591. https://doi.org/10.1007/s11055-010-9299-z.

Besnoff, J.S., Deyle, T., Harrison, R.R., Reynolds, M.S., 2013. Battery-free multichannel digital ECG biotelemetry using UHF RFID techniques. In: IEEE International Conference on RFID (RFID). Presented at the 2013 IEEE International Conference on RFID (RFID), pp. 16–22. 2013. https://doi.org/10.1109/RFID.2013.6548130.

Breidthardt, T., Christ, M., Matti, M., Schrafl, D., Laule, K., Noveanu, M., Boldanova, T., Klima, T., Hochholzer, W., Perruchoud, A.P., Mueller, C., 2007. QRS and QTc interval prolongation in the prediction of long-term mortality of patients with acute destabilized heart failure. Heart. https://doi.org/10.1136/hrt.2006.102319.

Bulling, A., Ward, J.A., Gellersen, H., Troster, G., 2011. Eye movement analysis for activity recognition using Electrooculography. IEEE Trans. Pattern Anal. Mach. Intell. 33, 741–753. https://doi.org/10.1109/TPAMI.2010.86.

Chan, A.D., Green, G.C., 2017. Myoelectric control development toolbox. CMBES Proc. 30.

Choi, S., Chae, J., 2009. A regenerative biosensing surface in microfluidics using electrochemical desorption of short-chain self-assembled monolayer. Microfluid. Nanofluidics 7, 819.

Chung, H.U., Kim, B.H., Lee, J.Y., Lee, J., Xie, Z., Ibler, E.M., Lee, K., Banks, A., Jeong, J.Y., Kim, J., 2019. Binodal, wireless epidermal electronic systems with in-sensor analytics for neonatal intensive care. Science 363 eaau0780.

Cockbain, A.G., Harrop, P.J., 1968. The temperature coefficient of capacitance. J. Phys. Appl. Phys. 1, 1109.

Darrell, T., Pentland, A., 1993. Recognition of space-time gestures using a distributed representation. Vision and modeling group, media laboratory, Massachusetts institute of technology.

Dementyev, A., Smith, J.R., 2013. A wearable UHF RFID-based EEG system. In: IEEE International Conference on RFID (RFID). Presented at the 2013 IEEE International Conference on RFID (RFID), pp. 1–7. 2013. https://doi.org/10.1109/RFID.2013.6548128.

Dey, N., Biswas, D., Roy, A.B., Das, A., Chaudhuri, S.S., 2012. DWT-DCT-SVD based blind watermarking technique of gray image in electrooculogram signal. In: Intelligent Systems Design and Applications (ISDA), 2012 12th International Conference on. IEEE, pp. 680–685.

Dodge, S., Karam, L., 2016. Understanding how image quality affects deep neural networks, in: 2016 eighth international conference on quality of multimedia experience (QoMEX). Presented at the 2016 eighth international conference on quality of multimedia experience (QoMEX). https://doi.org/10.1109/QoMEX.2016.7498955 1–6.

Fonseca, M.A., Allen, M.G., Kroh, J., White, J., 2006. Flexible wireless passive pressure sensors for biomedical applications, in: tech. Dig. Solid-state sensor, actuator, and microsystems workshop (hilton head 2006). pp. 37–42.

Goldenberg, I., Moss, A.J., Zareba, W., 2006. QT interval: how to measure it and what is “normal. J. Cardiovasc. Electrophysiol. 17, 333–336. https://doi.org/10.1111/j.1540-8167.2006.00408.x.

Groves, R., Stein, K., Harame, D., Jadus, D., 1996. Temperature dependence of Q in spiral inductors fabricated in a silicon-germanium/BiCMOS technology. In: Proceedings of the 1996 Bipolar/BiCMOS Circuits and Technology Meeting. IEEE, pp. 153–156.

Heide, W., Koenig, E., Trillenberg, P., Kömpf, D., Zee, D.S., 1999. Electrooculography: technical standards and applications. The international federation of clinical neurophysiology. Electroencephalogr. Clin. Neurophysiol. Suppl. 52, 223–240.

Hockman, C.H., Mauck Jr., H.P., Hoff, E.C., 1966. ECG changes resulting from cerebral stimulation: II. A spectrum of ventricular arrhythmias of sympathetic origin. Am. Heart J. 71, 695–700.

Hsu, C.-W., Chang, C.-C., Lin, C.-J., 2003. A Practical Guide to Support Vector Classification.

Inbar, G.F., Noujaim, A.E., 1984. On surface EMG spectral characterization and its application to diagnostic classification. IEEE Trans. Biomed. Eng. BME- 31, 597–604. https://doi.org/10.1109/TBME.1984.325303.

Israel, C.W., Grönefeld, G., Ehrlich, J.R., Li, Y.-G., Hohnloser, S.H., 2004. Long-term risk of recurrent atrial fibrillation as documented by an implantable monitoring device: implications for optimal patient care. J. Am. Coll. Cardiol. 43, 47–52. https://doi.org/10.1016/j.jacc.2003.08.027.

Iwasaki, M., Kellinghaus, C., Alexopoulos, A.V., Burgess, R.C., Kumar, A.N., Han, Y.H., Lüders, H.O., Leigh, R.J., 2005. Effects of eyelid closure, blinks, and eye movements on the electroencephalogram. Clin. Neurophysiol. 116, 878–885.

Karahan, S., Yildirum, M.K., Kirtac, K., Rende, F.S., Butun, G., Ekenel, H.K., 2016. How image degradations affect deep CNN-based face recognition? In: International Conference of the Biometrics Special Interest Group (BIOSIG). Presented at the 2016 International Conference of the Biometrics Special Interest Group (BIOSIG), pp. 1–5. 2016. https://doi.org/10.1109/BIOSIG.2016.7736924.

Kim, J.Banks, A.Xie, Z.Heo, S.Y.Gutruf, P.Lee, J.W.Xu, S.Jang, K.-I.Liu, F.Brown, G.Choi, J.Kim, J.H.Feng, X.Huang, Y.Paik, U.Rogers, J.A. n.d. Miniaturized flexible electronic systems with wireless power and near-field communication capabilities. Adv. Funct. Mater.25. https://doi.org/10.1002/adfm.201501590 4761–4767.

Kim, Jeonghyun, Salvatore, G.A., Araki, H., Chiarelli, A.M., Xie, Z., Banks, A., Sheng, X., Liu, Y., Lee, J.W., Jang, K.-I., Heo, S.Y., Cho, K., Luo, H., Zimmerman, B., Kim, Joonhee, Yan, L., Feng, X., Xu, S., Fabiani, M., Gratton, G., Huang, Y., Paik, U., Rogers, J.A., 2016. Battery-free, stretchable optoelectronic systems for wireless optical characterization of the skin. Sci. Adv. 2 e1600418. https://doi.org/10.1126/sciadv.1600418.

Kiranyaz, S., Ince, T., Gabbouj, M., 2016. Real-time patient-specific ECG classification by 1-D convolutional neural networks. IEEE Trans. Biomed. Eng. 63, 664–675. https://doi.org/10.1109/TBME.2015.2468589.

Lin, C.-H., 2008. Frequency-domain features for ECG beat discrimination using grey relational analysis-based classifier. Comput. Math. Appl. 55, 680–690. https://doi.org/10.1016/j.camwa.2007.04.035.

Liu, S., Navaei, A., Meng, X., Nikkhah, M., Chae, J., 2017. Wireless passive stimulation of engineered cardiac tissues. ACS Sens. 2, 1006–1012. https://doi.org/10.1021/acssensors.7b00279.

Mayer, R., Kress, H.-D., Migl, J., 2001. Antenna performance measurements at extreme temperatures. Eur. SPACE AGENCY-Publ. ESA SP 467, 377–382.

Pan, Y., Hu, N., Wei, X., Gong, L., Zhang, B., Wan, H., Wang, P., 2019. 3D cell-based biosensor for cell viability and drug assessment by 3D electric cell/matrigel-substrate impedance sensing. Biosens. Bioelectron. 130, 344–351.

Philipose, M., Smith, J.R., Jiang, B., Mamishev, A., Roy, S., Sundara-Rajan, K., 2005. Battery-free wireless identification and sensing. IEEE Pervasive Comput. 4, 37–45. https://doi.org/10.1109/MPRV.2005.7.

Phinyomark, A., Phukpattaranot, P., Limsakul, C., 2012. Feature reduction and selection for EMG signal classification. Expert. Syst. Appl. 39, 7420–7431. https://doi.org/10.1016/i.eswa.2012.01.102. https://doi.org/10.1016/i.eswa.2012.01.102.

Rainoldi, A., Melchiorri, G., Caruso, I., 2004. A method for positioning electrodes during surface EMG recordings in lower limb muscles. J. Neurosci. Methods 134, 37–43. https://doi.org/10.1016/j.jneumeth.2003.10.014.

Romhilt, D.W., Estes, E.H., 1968. A point-score system for the ECG diagnosis of left ventricular hypertrophy. Am. Heart J. 75, 752–758. https://doi.org/10.1016/0002-8703(68)90035-5.

Saitou, K., Masuda, T., Michikami, D., Kojima, R., Okada, M., 2000. Innervation zones of the upper and lower limb muscles estimated by using multichannel surface emg. J. Hum. Ergol. (Tokyo) 29, 35–52. https://doi.org/10.11183/jhe1972.29.35.

Schmidhuber, J., 2015. Deep learning in neural networks: an overview. Neural Network. 61, 85–117. https://doi.org/10.1016/j.neunet.2014.09.003.

Schwerdt, H.N., Miranda, F.A., Chae, J., 2015. Wireless fully passive multichannel recording of neuropotentials using photo-activated RF backscattering methods. IEEE Trans. Microw. Theory Tech. 63, 2965–2970. https://doi.org/10.1109/TMTT.2015.2460746.

Schwerdt, H.N., Miranda, F.A., Chae, J., 2013. Analysis of electromagnetic fields induced in operation of a wireless fully passive backscattering neurorecording microsystem in emulated human head tissue. IEEE Trans. Microw. Theory Tech. 61, 2170–2176. https://doi.org/10.1109/TMTT.2013.2252916.

Schwerdt, H.N., Miranda, F.A., Chae, J., 2012. A fully passive wireless backscattering neurorecording microsystem embedded in dispersive human-head phantom medium. IEEE Electron. Device Lett. 33, 908–910. https://doi.org/10.1109/LED.2012.2190967.

Schwerdt, H.N., Xu, W., Shekhar, S., Abbaspour-Tamijani, A., Towe, B.C., Miranda, F.A., Chae, J., 2011. A fully-passive wireless microsystem for recording of neuropotentials using RF backscattering methods. J. Microelectromechanical Syst. Jt. IEEE ASME Publ. Microstruct. Microactuators Microsens. Microsyst. 20, 1119–1130. https://doi.org/10.1109/JMEMS.2011.2162487.

Seo, D., Neely, R.M., Shen, K., Singhal, U., Alon, E., Rabaey, J.M., Carmena, J.M., Maharbiz, M.M., 2016. Wireless recording in the peripheral nervous system with ultrasonic neural dust. Neuron 91, 529–539.

Boach Thomsen, P.E., Jons, C., Raatikainen, M.P., Moerch Joergensen, R, Hartikainen, J., Virtanen, V., Boland, J., Anttonen, O., Gang, U.J., Hoest, N., Boersma, L.V.A., Platou, E.S., Becker, D., Messier, M.D., Huikuri, H.V., 2010. Long-term recording of cardiac arrhythmias with an implantable cardiac monitor in patients with reduced ejection fraction after acute myocardial InfarctionClinical perspective: the cardiac arrhythmias and risk stratification after acute myocardial infarction (CARISMA) study. Circulation 122, 1258–1264. https://doi.org/10.1161/CIRCULATIONAHA.109.902148.

Wang, R., Lajevardi-Khosh, A., Choi, S., Chae, J., 2011. Regenerative Surface Plasmon Resonance (SPR) biosensor: real-time measurement of fibrinogen in undiluted human serum using the competitive adsorption of proteins. Biosens. Bioelectron. 28, 304–307.

Wang, R., Wang, W., Ren, H., Chae, J., 2014. Detection of copper ions in drinking water using the competitive adsorption of proteins. Biosens. Bioelectron. 57, 179–185.

Wirdatmadja, S.A., Balasubramaniam, S., Koucheryavy, Y., Jornet, J.M., 2016. Wireless optogenetic neural dust for deep brain stimulation. In: IEEE 18th International Conference on E-Health Networking, Applications and Services (Healthcom). Presented at the 2016 IEEE 18th International Conference on e-Health Networking, Applications and Services, pp. 1–6. 2016. https://doi.org/10.1109/HealthCom.2016.7749532.

Xu, S., Zhang, Y., Jia, L., Mathewson, K.E., Jang, K.-I., Kim, J., Fu, H., Huang, X., Chava, P., Wang, R., Bhole, S., Wang, L., Na, Y.J., Guan, Y., Flavin, M., Han, Z., Huang, Y., Rogers, J.A., 2014. Soft microfluidic assemblies of sensors, circuits, and radios for the skin. Science 344, 70–74. https://doi.org/10.1126/science.1250169.

Yap, Y.G., Camm, A.J., 2003. Drug induced QT prolongation and torsades de pointes. Heart 89, 1363–1372. https://doi.org/10.1136/heart.89.11.1363.

Yeon, P., Mirbozorgi, S.A., Ash, B., Eckhardt, H., Ghovanloo, M., 2016. Fabrication and microassembly of a mm-sized floating probe for a distributed wireless neural interface. Micromachines 7, 154. https://doi.org/10.3390/mi7090154.

Zardoshti-Kermani, M., Wheeler, B.C., Badie, K., Hashemi, R.M., 1995. EMG feature evaluation for movement control of upper extremity prostheses. IEEE Trans. Rehabil. Eng. 3, 324–333. https://doi.org/10.1109/86.481972.

Zarnik, M.S., Belavic, D., 2012. An experimental and numerical study of the humidity effect on the stability of a capacitive ceramic pressure sensor. Radioengineering 21.

Zou, L., Wang, Q., Tong, M., Li, H., Wang, J., Hu, N., Wang, P., 2016. Detection of diarrhetic shellfish poisoning toxins using high-sensitivity human cancer cell-based impedance biosensor. Sensor. Actuator. B Chem. 222, 205–212.